applied sciences

MDPI

Communication

Wavefront Shaping-Assisted Forward-Viewing Photoacoustic Endomicroscopy Based on a Transparent Ultrasound Sensor

Tianrui Zhao [1,†], Mengjiao Zhang [1,2,†], Sebastien Ourselin [1] and Wenfeng Xia [1,*]

[1] School of Biomedical Engineering & Imaging Sciences, King's College London, 4th Floor, Lambeth Wing, St Thomas' Hospital, London SE1 7EH, UK
[2] School of Physics Science and Engineering, Tongji University, Institute of Acoustics, Shanghai 200092, China
* Correspondence: wenfeng.xia@kcl.ac.uk
† These authors contributed equally to this work.

Abstract: Photoacoustic endoscopy (PAE) can provide 3D functional, molecular and structural information of tissue deep inside the human body, and thus could be well suited for guiding minimally invasive procedures such as tumour biopsy and fetal surgery. One of the major challenges in the development of miniature PAE probes, in particular, forward-viewing PAE probes, is the integration of a sensitive and broadband ultrasound sensor with the light delivery and scanning system into a small footprint. In this work, we developed a forward-viewing PAE probe enabling optical-resolution microscopy imaging based on a transparent ultrasound sensor coated on the distal end of a multimode optical fibre. The transparent sensor comprised a transparent polyvinylidene fluoride (PVDF) thin film coated with indium tin oxide (ITO) electrodes with a diameter of 2 mm. Excitation laser light was focused and raster-scanned across the facet of the probe tip through the multimode fibre and the PVDF-ITO thin film via wavefront shaping. The sensor had an optical transmission rate of 55–72% in the wavelength range of 400 to 800 nm, a centre frequency of 17.5 MHz and a −10 dB bandwidth of 25 MHz. Singular value decomposition was used to remove a prominent trigger-induced noise, which enabled imaging close to the probe tip with an optically defined lateral resolution of 2 µm. The performance of the imaging probe was demonstrated by obtaining high-fidelity photoacoustic microscopy images of carbon fibres. With further optimisation of the sensitivity, the probe promises to guide minimally invasive procedures by providing in situ, in vivo characterisation of tissue.

Keywords: photoacoustic imaging; photoacoustic endoscopy; endomicroscopy; ultrasound; transparent piezoelectric transducer; wavefront shaping

check for updates

Citation: Zhao, T.; Zhang, M.; Ourselin, S.; Xia, W. Wavefront Shaping-Assisted Forward-Viewing Photoacoustic Endomicroscopy Based on a Transparent Ultrasound Sensor. *Appl. Sci.* **2022**, *12*, 12619. https://doi.org/10.3390/app122412619

Academic Editor: Filippo Giannazzo

Received: 16 November 2022
Accepted: 7 December 2022
Published: 9 December 2022

1. Introduction

Optical endoscopes are frequently used to examine internal organs and tissues such as colonoscopes, cystoscopes and bronchoscopes. However, conventional endoscopes with white-light-illumination only provide morphological information of superficial tissues and lack of molecular information of tissue. Advanced optical imaging modalities have been explored to provide comprehensive tissue characterisation [1]. Endoscopic optical coherence tomography (OCT) employs back-scattered light to visualise depth-resolved tissue morphology in real-time with micron-scale resolution. However, it is still challenging to distinguish between various tissue compositions owing to the lack of molecular specificity [2]. In contrast, fluorescence imaging offers molecular contrast by specifically exciting fluorescence light from fluorescent dyes or proteins that are labeled to target tissue compositions such tumour cells, but it is not straight forward to obtain depth-resolved tissue information [3].

Photoacoustic imaging (PAI) is a hybrid imaging modality that inherits advantages from both optical imaging and ultrasound imaging, combining rich optical absorption contrast and high spatial resolution from ultrasound. It has shown great potential in several

clinical disciplines such as oncology [4], dermatology [5–7] and cardiology [8]. Recent developments of photoacoustic endoscopy (PAE) have significantly extended the landscape of the clinical applicability of PAI to examining internal tissues [9,10]. Catheter-based side-viewing PAE has been the main research focus for imaging gastrointestinal tract tumours [11,12] and atherosclerotic plaques [13,14]. In contrast, forward-viewing probes are more suitable for guiding minimally invasive procedures such as needle biopsy, fetal surgery, and nerve blocks [15,16]. Optical fibres such as coherent bundles and multimode fibres are commonly used for delivery of the excitation light [17–24]. However, as conventional ultrasound detection usually relies on opaque piezoelectric transducers, a major challenge in the development of a miniature forward-viewing PAE probe has been the integration of the laser delivery module with the ultrasound detection module within a small space at the endoscopy probe tip. As a result, early studies employed transmission-mode implementations with the transducer placed between the light delivery fibre and tissue objects [17,18,20], which is not practical for clinical endoscopy applications.

Optical interferometry-based ultrasound sensors, owing to good optical transparency and broad acoustic bandwidths, have played an important role in the development of forward-viewing PAE probes. In 2018, Ansari et al. developed an all-optical forward-viewing PAE probes based on the photoacoustic computed tomography (PACT) principle [15], in which a dichromatic Fabry–Perot sensor was integrated at the distal tip of a rigid fibre bundle. Excitation laser (590 nm) was transmitted through the bundle and a continue wave laser (1500–1630 nm) was focused into and scanned across individual fibre cores to interrogate the sensor for ultrasound detection. High-fidelity 3D images of microvascular anatomies of animal and human tissues were obtained after tomographic image reconstructions. Recently, the same group further developed a flexible forward-viewing PAE by integrating a fibre bundle with a Fabry–Perot sensor using a miniature telecentric relay system [16,17]. In 2021, Keenlyside et al. reported a Fabry–Perot sensor coated multimode fibre as a smaller alternative to fibre bundles for endoscopic PACT [18]. The interrogation laser was raster-scanned via wavefront shaping through the multimode fibre for the detection of ultrasound.

Optical micro-resonator sensors were also integrated onto the tip of a single-mode fibre as sensitive and broadband miniature ultrasound sensors [25,26] and combined with multimode fibres for developing ultrathin PAE probes. Light transmission through the multimode fibre was controlled via the wavefront shaping technology [22,24,27], which enabled raster-scanning of a tightly focused laser beam in front of the fibre tip for an optical-resolution photoacoustic microscopy (OR-PAM) implementation. In a previous study, the authors group have reported a high-speed, high-fidelity photoacoustic endomicroscopy probe that was fitted into a 20-gauge needle for guiding minimally invasive surgery [28]. The probe comprised two optical fibres: a multimode fibre for delivering the excitation light and a single-mode fibre with a plano-concave micro-resonator for ultrasound detection. A tightly focused laser beam was raster-scanned through the multimode fibre with wavefront shaping using a digital micromirror device and a real-valued intensity transmission matrix-based algorithm [29,30], which enabled sub-cellular imaging of biological tissues at ~3 frames per second (fps).

Recently, transparent piezoelectric transducers have shown promise in PAI. Compared to optical ultrasound sensors, transparent piezoelectric transducers benefit from simple manufacturing and operational procedures, high stabilities, and low costs (compared to expensive interrogation lasers for optical ultrasound sensors). In 2005, Niederhauser et al. reported a transparent ITO-coated PVDF sensor for PAI [31]. In 2019, Li et al. reported a transparent capacitive micromachined ultrasonic transducers (CMUTs) using a glass substrate and ITO electrodes, which was demonstrated to detect optically excited ultrasound [32]. Dangi et al. fabricated transparent transducers by coating ITO onto lithium niobate ($LiNbO_3$) thin films and achieved PAI of artificial absorbers [33]. Most recently, several groups have demonstrated transparent transducers for photoacoustic microscopy of phantoms [34,35], animal vasculatures in skin [36–38], eyes [39], and brains [40].

In this work, for the first time to the best of our knowledge, we developed a forward-viewing PAE probe based on a transparent ultrasound sensor integrated at the tip of a multimode fibre. A focused laser beam was raster-scanned through the multimode fibre via wavefront shaping whilst the generated ultrasound was detected with the transparent sensor. Singular value decomposition (SVD) was used to eliminate a prominent trigger-induced noise. High-fidelity OR-PAM images of carbon fibres were achieved at varying distances to the probe distal end.

2. Materials and Methods

2.1. Transparent Senosr Fabrication

The transparent ultrasound sensor was based on a ITO-coated PVDF thin film (PolyK Technologies LLC, Philipsburg, PA, USA). The PVDF thin film had a thickness of 50 µm and was coated with a 200-Ohm ITO electrode on each surface. The thin film was firstly cropped into a ~4 mm × 4 mm square, which was then affixed onto the tip of brass tube (diameter: 2 mm; length: 3 cm) with electrically conductive epoxy (RS PRO Liquid Adhesive, Northamptonshire, UK). After the conductive epoxy was cured (24 h at room temperature), the PVDF-ITO thin film around the brass tube was trimmed. The wall thickness of the brass tube was 0.5 mm resulting in a transparent window with a diameter of 1 mm through the brass tube (Figure 1). The core of a micro-coaxial electrical cable tip was connected onto the top surface of the PVDF-ITO thin film, whilst its outer electrical wire was connected to the brass tube wall with the electrically conductive epoxy. The other tip of the electrical cable was connected to a BNC connector which was then connected to a pre-amplifier (SPA.1411, Sprectrum Instrumentation, Grosshansdorf, Germany). The transmittance of light (400–800 nm) through the sensor was measured using a custom spectrophotometre. The frequency response of the transparent ultrasound sensor was characterised by detecting optically generated ultrasound signals from a black tape.

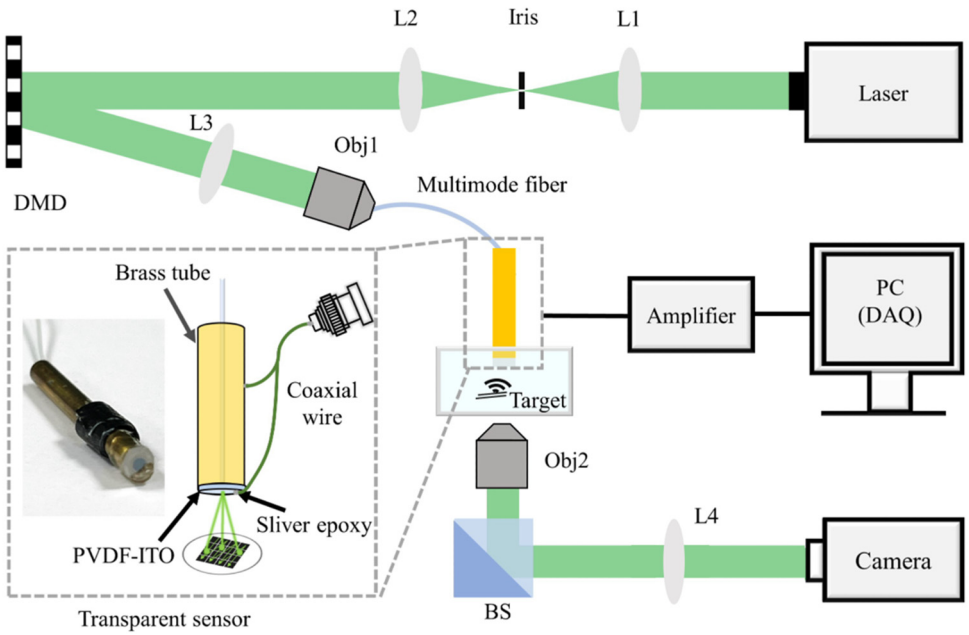

Figure 1. Schematic diagram of the photoacoustic endomicroscopy imaging system. The inset shows a photograph and a schematic of the transparent ultrasound sensor. DMD, digital micromirror device; L1–L2, convex lens (f = 50 mm); L3–4 convex lens (f = 100 mm); Obj1–2, objective lenses; BS, beamsplitter; DAQ, data acquisition card.

2.2. Imaging System

The photoacoustic endomicroscopy imaging system is illustrated in Figure 1. A 532 nm pulsed laser (2 ns, SPOT-10-200-532, Elforlight, Northamptonshire, UK) was used as the

excitation light source. The light wavefront was modulated by a digital micromirror device (DMD, DLP7000, Texas Instruments, Dallas, TX, USA) before projected onto the proximal tip of a multimode fibre (core diameter: 100 μm; NA: 0.29; length: 30 cm) through a convex lens (AC254-050-A-ML, Thorlabs, Newton, NJ, USA) and an objective (0.4 NA, RMS20X, Newton, NJ, USA). The distal end of the multimode fibre was integrated within the brass tube with the fibre tip attached to the PVDF-ITO thin film at the centre.

Since the light transport through a multimode fibre is scrambled by mode dispersion, a fibre characterisation process was implemented before imaging with wavefront shaping, which was detailed in our previous works [29,30]. Here, briefly, a series of binary patterns were displayed on the DMD while the corresponding output speckles through the multimode fibre and the sensor were recorded with a camera. With these input-output pairs, the light intensity changes from the DMD to the distal fibre tip was modelled as a real-valued intensity transmission matrix (RVITM), achieved via direct matrix manipulations. Then, optimal DMD patterns that led to light focusing through the multimode fibre were calculated from the RVITM. As such, raster-scanning a tightly focused laser beam across the distal fibre tip was performed by sequentially displaying these optimal DMD patterns. The characterisation module comprising a camera, a beamsplitter and lenses was removed after fibre characterisation. For imaging, the sensor was immersed in a water tank, and samples were placed at various depths in front of the distal multimode fibre tip. The focal plane of the imaging probe was defined during the characterisation process by adjusting the focal plane of the camera accordingly. For each scanning position, a photoacoustic signal was excited from the sample, and then received by the sensor and recorded by a data acquisition card (M4i.4420, 250 MHz, Spectrum Instrumentation, Grosshansdorf, Germany) after amplification. Maximum intensity projection PAM images were formed by showing the peak-to-peak amplitudes of the ultrasound signals.

2.3. SVD Denoising

Received radio-frequency signals had a strong trigger-induced noise that spans from 0 to 0.50 μs corresponding to a distance from 0 to 0.75 mm to the sensor surface (Figure 2). This signal was relatively consistent across different scanning positions and manifested as vertical lines in the raw signals matrix (Figure 2). One way to avoid the interference of the noise is to move the focal plane away from this region (greater than 0.75 mm depth), however, this approach sacrifices the achievable spatial resolution with a multimode fibre. Here, SVD was used to address this issue. SVD has been demonstrated to remove laser-induced noise and background thermal noise in photoacoustic imaging [41,42]. Briefly, the 2D raw signals matrix X (time-varying signals acquired at different spatial locations) was decomposed with SVD as:

$$\mathbf{X = USV^T} \quad (1)$$

where S is the diagonal matrix of singular values that are sorted in declining order, and U and V are matrices of the left- and right-singular vectors, respectively. The raw signals matrix is assumed to comprise three main components as:

$$\mathbf{X = X_t + X_{pa} + \varepsilon} \quad (2)$$

where X_t represents the trigger-induced noise, X_{pa} is the photoacoustic signal generated from tissue, and ε is the residual thermal noise. Since electrical triggers caused strong and almost constant noises across all A-line signals, these compositions have relatively high coherence and thus tend to be acquired in the singular vectors with the largest singular values. Similarly, the thermal noise can be considered random, and corresponds to the

singular vectors with small singular values. So, X_{pa} can be preserved by assigning the first n and the last k singular values as zero in the new diagonal matrix of singular values S_a as:

$$S_a(i) = \begin{cases} 0, \ 1 \leq i \leq n \\ S(i), \ n < i \leq k \\ 0, \ i > k \end{cases} \tag{3}$$

and the filtered ultrasound signals can be reconstructed via:

$$\mathbf{X'} = \mathbf{US_aV^T} \tag{4}$$

where X′ is the denoised signals matrix, each column of which represents an A-line photoacoustic signal.

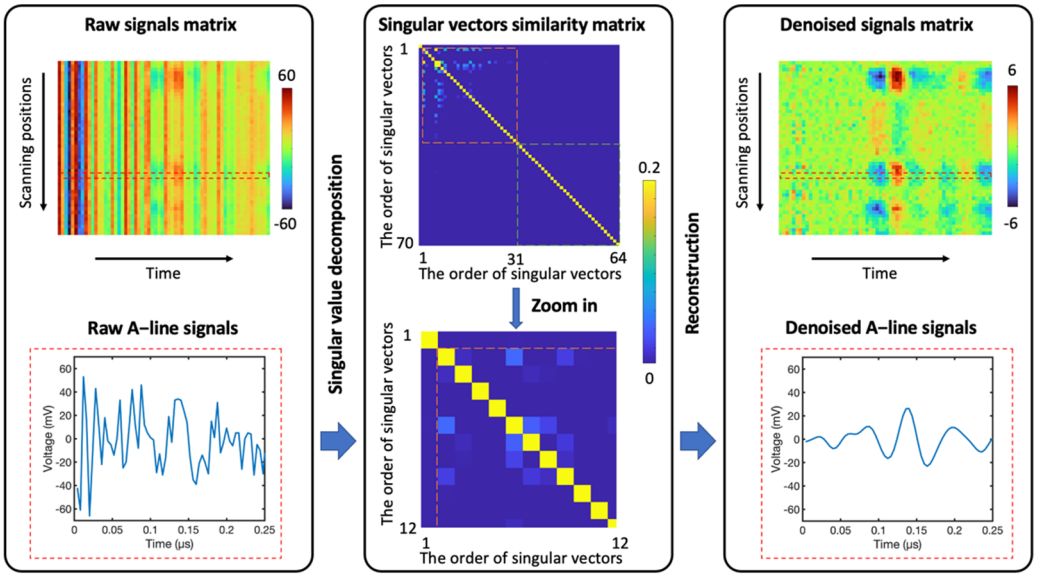

Figure 2. Workflow of singular value decomposition denoising to retrieve photoacoustic signals that were significantly distorted by the trigger-induced noise. A set of A-line signals received by the sensor form a raw signals matrix. After singular value decomposition of this matrix, the correlation coefficients between left-singular vectors are calculated and grouped into three sub-areas. The first sub−area is the first vector which only has coherence to itself and corresponds to the trigger-induced noise. The second sub-area (orange box) contains vectors with coherence to neighborhood vectors and corresponds to photoacoustic signals. The third sub-area (green box) that corresponds to small singular values and shows no coherence to other vectors contains random noises.

Similarity matrices of the spatial vectors were used to determine which singular values and vectors to be removed as described in Ref. [43]. Here, correlation coefficients of left-singular vectors were calculated and formed a matrix with each coefficient representing the similarity between each two vectors. Due to different coherence associated with X_t, X_{pa} and ε, the similarity matrix is expected to be separated into 3 distinct areas. In the case shown in Figure 2, the vectors that contained X_{pa} (in the orange box) had observable correlation coefficients, whilst the 1st vector showed coherence only to itself represented X_t, and other vectors referred to random noise ε (in the green box). Thus, we kept only the singular vectors corresponding to the singular vectors in the orange box in the new diagonal matrix S_a to reconstruct ultrasound signals.

3. Results

3.1. Sensor Characterisation

The PVDF-ITO thin film had a transmittance of 55–72% in the wavelength range from 400 nm to 800 nm, as shown in Figure 3a. With the excitation laser light at 532 nm, the sensor had a transmission of 63%. The frequency response was evaluated by receiving a photoacoustic signal generated from a black tape, which was placed ~1 mm away from the sensor tip to separate the signal from the trigger-induced noise (Figure 3b). The power spectrum of the photoacoustic signal indicated that the transparent ultrasound sensor had a centre frequency of 17.5 MHz, and a −10 dB bandwidth of 5–30 MHz (Figure 3c).

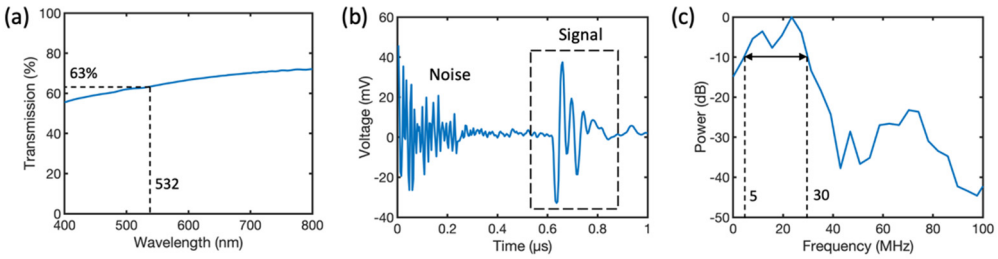

Figure 3. Optical and acoustic characteristics of the transparent ultrasound sensor. (**a**) Light transmittance through the PVDF−ITO thin film. (**b**) Detected photoacoustic signal from a black tap placed ~1 mm away from the transparent ultrasound sensor and the trigger-induced noise. (**c**) Power spectrum of the detected photoacoustic signal (in the dash box in (**b**)).

3.2. Photoacoustic Microscopy Imaging

OR-PAM imaging was performed at three imaging planes with various distances (200 μm, 320 μm and 620 μm) from the multimode fibre tip to study the impact of the trigger-induced noise. Since attaching the electrical wire onto the top surface of the PVDF-ITO thin film resulted in a ~200-μm-thick bump on the sensor surface and the thin film had a thickness of 50 μm, the nearest imaging plane was set 250 μm away from the fibre tip. In this plane, the received ultrasound signals were significantly distorted by strong noise induced by triggers. Here, we used the distance from the sample to the PVDF thin film to characterise the multimode fibre for laser scanning in the imaging plane. The light focus achieved with wavefront shaping, which defined the image resolution, gradually worsened from 2 μm to 3.7 μm (Figure 4) with the distance increasing from 200 μm (attached the electrical wire bump) to 620 μm. This observation can be attributed to the decrease of the effective fibre numerical aperture with the increase of the distance from the fibre tip.

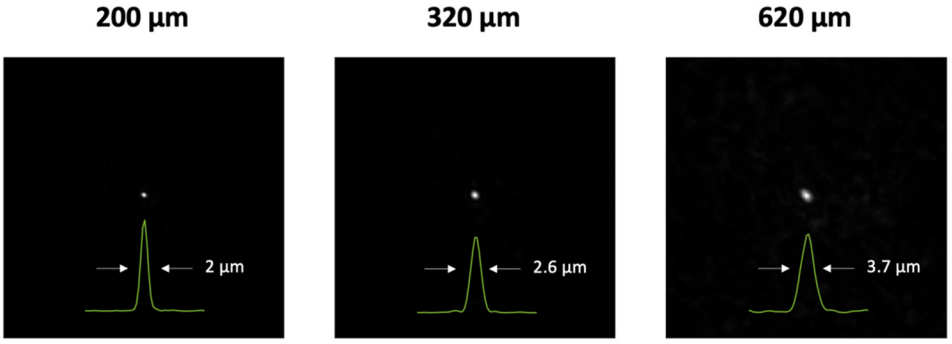

Figure 4. Light foci at various distances from the optical fibre tip.

Figure 5 shows the received photoacoustic signals (before and after SVD denoising), and OR-PAM images of carbon fibres acquired at three imaging planes. The laser energy transmitted from the distal fibre tip was measured as ~100 nJ. The focused laser was raster-scanned with a step of 1.5 μm. Each image comprised 100 × 100 pixels representing a

field-of-view of 150 µm × 150 µm. The raw photoacoustic signals were firstly averaged over 64 repeated measurements and raw images were formed using the peak-to-peak amplitudes of averaged raw ultrasound signals. With the DMD running at a frame rate of 22.7 kHz, it took ~28 s to acquire each image. Images achieved with the SVD filter clearly visualised the structures of the carbon fibre networks, which are consistent with the images of the phantoms acquired with optical microscopy.

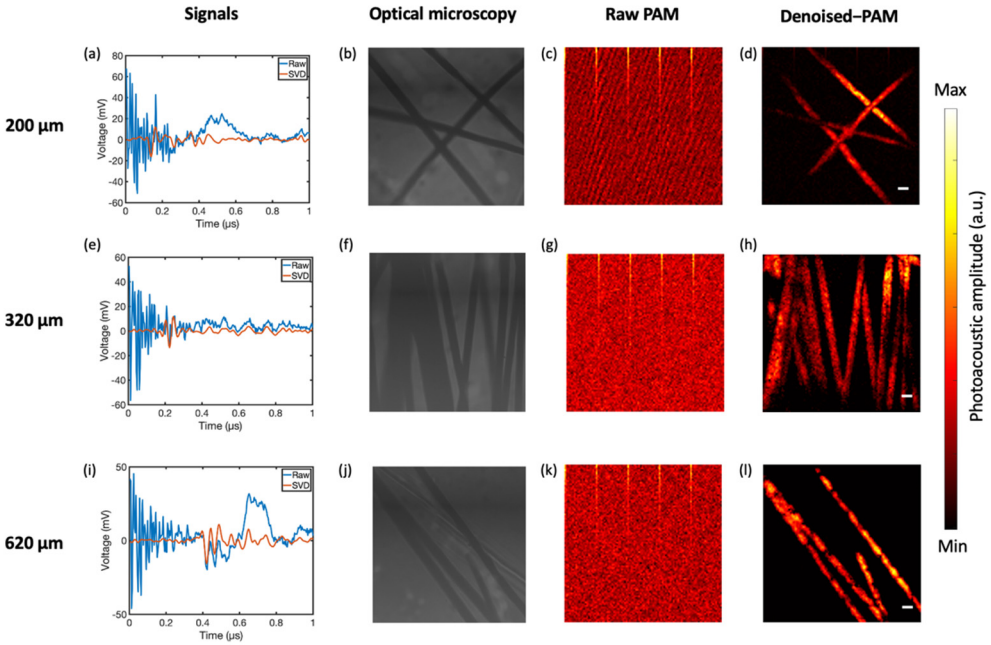

Figure 5. Examples of photoacoustic microscopy (PAM) images of carbon fibres acquired with the developed imaging probe. Images on the left column are detected ultrasound signals before and after the singular value decomposition (SVD) denoising at different imaging planes with the distance from the probe tip of 200 µm (**a**), 320 µm (**e**) and 620 µm (**i**). (**b**,**f**,**j**) are optical microscopy images of carbon fibre networks at different imaging planes. The right two columns are PAM images before and after SVD denoising at 200 µm (**c**,**d**), 320 µm (**g**,**h**) and 620 µm (**k**,**l**). Scale bars represent 10 µm.

4. Discussion

We developed an optical-resolution forward-viewing photoacoustic endomicroscopy probe based on an optically transparent ultrasound sensor using a ITO-coated PVDF thin film. Although transparent ultrasound sensors have been used in PAI in recent years, this work is the first study, to the best of our knowledge, that a transparent piezoelectric sensor is used in PAE. The outer diameter of the endomicroscopy probe is 2 mm defined by the diameter of the transparent sensor, which can be further reduced towards the diameter of a multimode fibre. With future optimisation, such a forward-viewing probe could be well suited for the guidance of minimally invasive procedures such as fetal surgery and tumour biopsy.

Although optical ultrasound sensors possess several distinct advantages such as large bandwidths, and high sensitivity with miniature footprints, the transparent PVDF-ITO sensor benefits from a simple manufacturing process, a high stability, and a low cost. The optical transparency of the PVDF-ITO sensor also facilitates the integration of PAM with other optical imaging modalities such as confocal, fluorescence, two-photon, and Raman imaging to provide more comprehensive information of tissue. Compared to LiNbO3, PVDF transducers benefit from lower acoustic impedance mismatch with tissue, higher frequency bandwidths and greater flexibility.

It is significant to be able to set the imaging plane close to the fibre tip as a large numerical aperture can thus be retained for high spatial resolution. In this work, the closest distance to the PVDF thin film that the imaging sample can be placed was 200 µm due to the

conductive epoxy and electrical wire attached on the PVDF surface. The SVD filter was able to eliminate trigger-induced electrical noises which overwhelmed photoacoustic signals generated from objects close to the sensor (200–620 nm), which substantially improved the spatial resolution of the imaging probe from 3.7 to 2.0 μm as indicated by the sizes of the optical foci at different imaging planes (Figure 5). The PVDF had a thickness of ~50 μm and a −10 dB bandwidth of 25 MHz. A thinner PVDF film will provide a larger bandwidth and thus a higher axial resolution for 3D imaging.

High-resolution OR-PAM imaging has been demonstrated on phantoms comprising carbon fibres. In future works, the performance, such as the imaging depth of the imaging probe, will need to be tested on an in vivo animal model towards clinical translation. A pre-amplifier could be developed to improve the signal-to-noise ratio, which has been demonstrated effective in a benchtop PAM configuration [3]. In addition, better electrical grounding and shielding of the sensor could also be developed to reduce environmental noise. Another challenge for future clinical translation is related to fibre bending. Since the light transport through multimode fibres needs to be characterised before imaging, significant geometry changes degrade light focusing performance and thus the imaging quality. Potential solutions include employing a bending-insensitive fibre or computationally correcting the bending-induced distortions as demonstrated in previous studies [44,45].

5. Conclusions

In summary, we developed a miniature photoacoustic endomicroscopy imaging probe with a multimode fibre to deliver the excitation laser and a transparent ultrasound sensor to detect ultrasound signals. SVD was employed to eliminate the trigger-induced noise and improve the spatial resolution. With high-fidelity OR-PAM images obtained with carbon fibre phantoms, the developed imaging probe promises to provide in situ tissue characterisation towards optical biopsy.

Author Contributions: Conceptualization, T.Z. and W.X.; methodology, T.Z., M.Z. and W.X.; software, T.Z.; validation, T.Z. and M.Z.; formal analysis, T.Z., M.Z. and W.X.; investigation, T.Z. and W.X.; Data curation, T.Z. and W.X.; resources, S.O. and W.X.; writing—original draft preparation, T.Z. and M.Z.; writing—review and editing, All; supervision, W.X.; funding acquisition, S.O. and W.X. All authors have read and agreed to the published version of the manuscript.

Funding: This research was funded by the Academy of Medical Sciences/the Wellcome Trust/the Government Department of Business, Energy and Industrial Strategy/the British Heart Foundation/Diabetes UK Springboard Award [SBF006/1136], Wellcome Trust, United Kingdom (203148/Z/16/Z, WT101957) and Engineering and Physical Sciences Research Council, United Kingdom (NS/A000027/1, NS/A000049/1). For the purpose of open access, the authors have applied a CC BY public copyright license to any author-accepted manuscript version arising from this submission.

Institutional Review Board Statement: Not applicable.

Informed Consent Statement: Not applicable.

Data Availability Statement: The data that support the findings of this study are available on request from the corresponding author.

Acknowledgments: The authors thank Sacha Noimark from University College London, UK, for measuring the optical transmittance of the sensor. We thank Yadong Xu and Bao Xiao from the Northwestern Polytechnical University, China for insightful discussions on transparent sensor development.

Conflicts of Interest: S.O. is shareholder and co-founder of Hypervision Surgical.

References

1. Wang, T.D.; Van Dam, J. Optical Biopsy: A New Frontier in Endoscopic Detection and Diagnosis. *Clin. Gastroenterol. Hepatol.* **2004**, *2*, 744–753. [CrossRef] [PubMed]
2. Gora, M.J.; Suter, M.J.; Tearney, G.J.; Li, X. Endoscopic Optical Coherence Tomography: Technologies and Clinical Applications [Invited]. *Biomed. Opt. Express* **2017**, *8*, 2405. [CrossRef] [PubMed]

3. Mavadia, J.; Xi, J.; Chen, Y.; Li, X. An All-Fiber-Optic Endoscopy Platform for Simultaneous OCT and Fluorescence Imaging. *Biomed. Opt. Express* **2012**, *3*, 2851. [CrossRef] [PubMed]
4. Diot, G.; Metz, S.; Noske, A.; Liapis, E.; Schroeder, B.; Ovsepian, S.V.; Meier, R.; Rummeny, E.; Ntziachristos, V. Multispectral Optoacoustic Tomography (MSOT) of Human Breast Cancer. *Clin. Cancer Res.* **2017**, *23*, 6912–6922. [CrossRef] [PubMed]
5. Oh, J.-T.; Li, M.-L.; Zhang, H.F.; Maslov, K.; Stoica, G.; Wang, L.V. Three-Dimensional Imaging of Skin Melanoma in Vivo by Dual-Wavelength Photoacoustic Microscopy. *J. Biomed. Opt.* **2006**, *11*, 034032. [CrossRef] [PubMed]
6. Moothanchery, M.; Bi, R.; Kim, J.; Balasundaram, G.; Kim, C.; Olivo, M. High-speed simultaneous multiscale photoacoustic microscopy. *J. Biomed. Opt.* **2019**, *24*, 8. [CrossRef]
7. Bi, R.; Dinish, U.S.; Goh, C.; Imai, T.; Moothanchery, M.; Li, X.; Kim, J.; Jeon, S.; Pu, Y.; Kim, C.; et al. In vivo label-free functional photoacoustic monitoring of ischemic reperfusion. *J. Biophotonics* **2019**, *12*, 7. [CrossRef]
8. Jansen, K.; Oosterhuis, J.W.; van Soest, G. Intravascular Photoacoustic Imaging of Human Coronary Atherosclerosis. *Opt. Lett.* **2011**, *36*, 597–599. [CrossRef]
9. Zhao, T.; Desjardins, A.E.; Ourselin, S.; Vercauteren, T.; Xia, W. Minimally Invasive Photoacoustic Imaging: Current Status and Future Perspectives. *Photoacoustics* **2019**, *16*, 100146. [CrossRef]
10. Zhou, J.; Jokerst, J.V. Photoacoustic Imaging with Fiber Optic Technology: A Review. *Photoacoustics* **2020**, *20*, 100211. [CrossRef]
11. Yang, J.-M.; Favazza, C.; Chen, R.; Yao, J.; Cai, X.; Maslov, K.; Zhou, Q.; Shung, K.K.; Wang, L.V. Simultaneous Functional Photoacoustic and Ultrasonic Endoscopy of Internal Organs in vivo. *Nat. Med.* **2012**, *18*, 1297–1302. [CrossRef] [PubMed]
12. Li, Y.; Zhu, Z.; Jing, J.C.; Chen, J.J.; Heidari, A.E.; He, Y.; Zhu, J.; Ma, T.; Yu, M.; Zhou, Q.; et al. High-Speed Integrated Endoscopic Photoacoustic and Ultrasound Imaging System. *IEEE J. Select. Topics Quantum Electron.* **2019**, *25*, 1–5. [CrossRef]
13. Wang, P.; Ma, T.; Slipchenko, M.N.; Liang, S.; Hui, J.; Shung, K.K.; Roy, S.; Sturek, M.; Zhou, Q.; Chen, Z.; et al. High-Speed Intravascular Photoacoustic Imaging of Lipid-Laden Atherosclerotic Plaque Enabled by a 2-KHz Barium Nitrite Raman Laser. *Sci. Rep.* **2014**, *4*, 6889. [CrossRef] [PubMed]
14. Wu, M.; Springeling, G.; Lovrak, M.; Mastik, F.; Iskander-Rizk, S.; Wang, T.; van Beusekom, H.M.M.; van der Steen, A.F.W.; Van Soest, G. Real-Time Volumetric Lipid Imaging in Vivo by Intravascular Photoacoustics at 20 Frames per Second. *Biomed. Opt. Express* **2017**, *8*, 943. [CrossRef] [PubMed]
15. Ansari, R.; Zhang, E.Z.; Desjardins, A.E.; Beard, P.C. All-Optical Forward-Viewing Photoacoustic Probe for High-Resolution 3D Endoscopy. *Light Sci. Appl.* **2018**, *7*, 75. [CrossRef]
16. Ansari, R.; Zhang, E.Z.; Desjardins, A.E.; Beard, P.C. Miniature All-Optical Flexible Forward-Viewing Photoacoustic Endoscopy Probe for Surgical Guidance. *Opt. Lett.* **2020**, *45*, 6238. [CrossRef]
17. Ansari, R.; Zhang, E.Z.; Desjardins, A.E.; David, A.L.; Beard, P.C. Use of a Flexible Optical Fibre Bundle to Interrogate a Fabry–Perot Sensor for Photoacoustic Imaging. *Opt. Express* **2019**, *27*, 37886. [CrossRef]
18. Keenlyside, B.; Marques, D.; Cherkashin, M.; Zhang, E.; Munro, P.; Beard, P.; Guggenheim, J. Wavefront shaping through multimode fibres to enable endoscopic photoacoustic tomography. In Proceedings of the Adaptive Optics and Wavefront Control for Biological Systems VII, California, CA, USA, 6–12 March 2021; Volume 11652.
19. Hajireza, P.; Shi, W.; Zemp, R.J. Label-Free in Vivo Fiber-Based Optical-Resolution Photoacoustic Microscopy. *Opt. Lett.* **2011**, *36*, 4107. [CrossRef]
20. Shao, P.; Shi, W.; Hajireza, P.; Zemp, R.J. Integrated Micro-Endoscopy System for Simultaneous Fluorescence and Optical-Resolution Photoacoustic Imaging. *J. Biomed. Opt.* **2012**, *17*, 0760241. [CrossRef]
21. Li, G.; Guo, Z.; Chen, S.-L. Miniature Probe for Forward-View Wide-Field Optical-Resolution Photoacoustic Endoscopy. *IEEE Sensors J.* **2019**, *19*, 909–916. [CrossRef]
22. Papadopoulos, I.N.; Simandoux, O.; Farahi, S.; Pierre Huignard, J.; Bossy, E.; Psaltis, D.; Moser, C. Optical-Resolution Photoacoustic Microscopy by Use of a Multimode Fiber. *Appl. Phys. Lett.* **2013**, *102*, 211106. [CrossRef]
23. Stasio, N.; Shibukawa, A.; Papadopoulos, I.N.; Farahi, S.; Simandoux, O.; Huignard, J.-P.; Bossy, E.; Moser, C.; Psaltis, D. Towards New Applications Using Capillary Waveguides. *Biomed. Opt. Express* **2015**, *6*, 4619. [CrossRef] [PubMed]
24. Mezil, S.; Caravaca-Aguirre, A.M.; Zhang, E.Z.; Moreau, P.; Wang, I.; Beard, P.C.; Bossy, E. Single-Shot Hybrid Photoacoustic-Fluorescent Microendoscopy through a Multimode Fiber with Wavefront Shaping. *Biomed. Opt. Express* **2020**, *11*, 5717. [CrossRef] [PubMed]
25. Guggenheim, J.A.; Li, J.; Allen, T.J.; Colchester, R.J.; Noimark, S.; Ogunlade, O.; Parkin, I.P.; Papakonstantinou, I.; Desjardins, A.E.; Zhang, E.Z.; et al. Ultrasensitive Plano-Concave Optical Microresonators for Ultrasound Sensing. *Nat. Photon.* **2017**, *11*, 714–719. [CrossRef]
26. Allen, T.J.; Ogunlade, O.; Zhang, E.; Beard, P.C. Large Area Laser Scanning Optical Resolution Photoacoustic Microscopy Using a Fibre Optic Sensor. *Biomed. Opt. Express* **2018**, *9*, 650. [CrossRef]
27. Zhao, T.; Ma, M.T.; Ourselin, S.; Vercauteren, T.; Xia, W. Video-Rate Dual-Modal Photoacoustic and Fluorescence Imaging through a Multimode Fibre towards Forward-Viewing Endomicroscopy. *Photoacoustics* **2022**, *25*, 100323. [CrossRef]
28. Zhao, T.; Pham, T.T.; Baker, C.; Ma, M.T.; Ourselin, S.; Vercauteren, T.; Zhang, E.; Beard, P.C.; Xia, W. Ultrathin, High-Speed, All-Optical Photoacoustic Endomicroscopy Probe for Guiding Minimally Invasive Surgery. *Biomed. Opt. Express* **2022**, *13*, 4414. [CrossRef]
29. Zhao, T.; Ourselin, S.; Vercauteren, T.; Xia, W. Seeing through Multimode Fibers with Real-Valued Intensity Transmission Matrices. *Opt. Express* **2020**, *28*, 20978. [CrossRef]

30. Zhao, T.; Ourselin, S.; Vercauteren, T.; Xia, W. Focusing Light through Multimode Fibres Using a Digital Micromirror Device: A Comparison Study of Non-Holographic Approaches. *Opt. Express* **2021**, *29*, 14269. [CrossRef]
31. Niederhauser, J.J.; Jaeger, M.; Hejazi, M.; Keppner, H.; Frenz, M. Transparent ITO Coated PVDF Transducer for Optoacoustic Depth Profiling. *Opt. Commun.* **2005**, *253*, 401–406. [CrossRef]
32. Li, Z.; Ilkhechi, A.K.; Zemp, R. Transparent Capacitive Micromachined Ultrasonic Transducers (CMUTs) for Photoacoustic Applications. *Opt. Express* **2019**, *27*, 13204. [CrossRef] [PubMed]
33. Dangi, A.; Agrawal, S.; Kothapalli, S.-R. Lithium Niobate-Based Transparent Ultrasound Transducers for Photoacoustic Imaging. *Opt. Lett.* **2019**, *44*, 5326. [CrossRef] [PubMed]
34. Fang, C.; Hu, H.; Zou, J. A Focused Optically Transparent PVDF Transducer for Photoacoustic Microscopy. *IEEE Sens. J.* **2020**, *20*, 2313–2319. [CrossRef]
35. Kashani Ilkhechi, A.; Ceroici, C.; Dew, E.; Zemp, R. Transparent Capacitive Micromachined Ultrasound Transducer Linear Arrays for Combined Realtime Optical and Ultrasonic Imaging. *Opt. Lett.* **2021**, *46*, 1542. [CrossRef] [PubMed]
36. Chen, R.; He, Y.; Shi, J.; Yung, C.; Hwang, J.; Wang, L.V.; Zhou, Q. Transparent High-Frequency Ultrasonic Transducer for Photoacoustic Microscopy Application. *IEEE Trans. Ultrason. Ferroelect. Freq. Contr.* **2020**, *67*, 1848–1853. [CrossRef]
37. Fang, C.; Zou, J. Acoustic-Resolution Photoacoustic Microscopy Based on an Optically Transparent Focused Transducer with a High Numerical Aperture. *Opt. Lett.* **2021**, *46*, 3280. [CrossRef] [PubMed]
38. Liu, Y.-H.; Kurnikov, A.; Li, W.; Kazakov, V.; Ni, R.; Subochev, P.; Razansky, D. Sensitive Ultrawideband Transparent PVDF-ITO Ultrasound Detector for Optoacoustic Microscopy. *Opt. Lett.* **2022**, *47*, 4163. [CrossRef]
39. Park, J.; Park, B.; Kim, T.Y.; Jung, S.; Choi, W.J.; Ahn, J.; Yoon, D.H.; Kim, J.; Jeon, S.; Lee, D.; et al. Quadruple Ultrasound, Photoacoustic, Optical Coherence, and Fluorescence Fusion Imaging with a Transparent Ultrasound Transducer. *Proc. Natl. Acad. Sci. USA* **2021**, *118*, e1920879118. [CrossRef]
40. Mirg, S.; Chen, H.; Turner, K.L.; Gheres, K.W.; Liu, J.; Gluckman, B.J.; Drew, P.J.; Kothapalli, S.-R. Awake Mouse Brain Photoacoustic and Optical Imaging through a Transparent Ultrasound Cranial Window. *Opt. Lett.* **2022**, *47*, 1121. [CrossRef]
41. Hill, E.R.; Xia, W.; Clarkson, M.J.; Desjardins, A.E. Identification and Removal of Laser-Induced Noise in Photoacoustic Imaging Using Singular Value Decomposition. *Biomed. Opt. Express* **2017**, *8*, 68. [CrossRef]
42. Baranger, J.; Arnal, B.; Perren, F.; Baud, O.; Tanter, M.; Demene, C. Adaptive Spatiotemporal SVD Clutter Filtering for Ultrafast Doppler Imaging Using Similarity of Spatial Singular Vectors. *IEEE Trans. Med. Imaging* **2018**, *37*, 1574–1586. [CrossRef] [PubMed]
43. Shi, M.; Vercauteren, T.; Xia, W. Spatiotemporal singular value decomposition for denoising in photoacoustic imaging with low-energy excitation light source. *Biomed. Opt. Express* **2022**, *13*, 6416. [CrossRef]
44. Boonzajer Flaes, D.E.; Stopka, J.; Turtaev, S.; de Boer, J.F.; Tyc, T.; Čižmár, T. Robustness of Light-Transport Processes to Bending Deformations in Graded-Index Multimode Waveguides. *Phys. Rev. Lett.* **2018**, *120*, 233901. [CrossRef] [PubMed]
45. Tsvirkun, V.; Sivankutty, S.; Baudelle, K.; Habert, R.; Bouwmans, G.; Vanvincq, O.; Andresen, E.R.; Rigneault, H. Flexible Lensless Endoscope with a Conformationally Invariant Multi-Core Fiber. *Optica* **2019**, *6*, 1185. [CrossRef]